ACS APPLIED NANO MATERIALS

Open Access

www.acsanm.org

Article

3D-Printed Graphene and Graphene Quantum Dot-Reinforced Polycaprolactone Scaffolds for Bone-Tissue Engineering

Duo Meng,[§] Yanhao Hou,[§] Darwin Kurniawan, Ren-Jie Weng, Wei-Hung Chiang, and Weiguang Wang*

Cite This: *ACS Appl. Nano Mater.* 2024, 7, 1245−1256

Read Online

ACCESS | Metrics & More | Article Recommendations

ABSTRACT: The regeneration of large-scale bone loss due to accidents, trauma, diseases, or tumor resection is still a critical clinical challenge. With the development of additive manufacturing technology and advanced biomaterials, 3D-printed biocompatible synthetic polymer scaffolds have been widely studied for their key roles in supporting bone tissue regeneration. Scaffold aims to provide mechanical properties that match the host bone as well as biological activities that can effectively promote cell proliferation and differentiation, ultimately facilitating bone tissue regeneration. Due to its unique biocompatibility and biodegradability, polycaprolactone (PCL) becomes one of the dominant synthetic polymeric materials considered for scaffold fabrication. However, using PCL alone presents insufficient mechanical properties; thus, different functional fillers have been added to modulate both the mechanical and biological performance of fabricated scaffolds. Among all functional fillers, carbon nanomaterials, particularly graphene (G), have shown an emerging trend. Graphene quantum dots (GQD), a member of the graphene family, are regarded as an ideal next-generation functional filler for scaffold fabrication. It presents high solubility in water, controllable dose-dependent cytotoxicity similar to that of G, and unique biological properties benefiting from smaller sizes. Current research using GQD for tissue engineering applications is limited, and the systemic comparison between G and GQD at different concentrations is also missing. This study, for the first time, evaluates and compares the impact of incorporating G and GQD into PCL bone tissue engineering scaffolds from surface, thermal, mechanical, and biological perspectives. Results suggested that the addition of both materials under 5 wt % significantly improved both the mechanical and biological performance of PCL scaffolds. Under 3 wt %, PCL/GQD scaffolds presented better compressive strength while maintaining the same level of biological performance compared with PCL/G scaffolds, revealing the strong potential for future *in vivo* studies and bone tissue regeneration applications.

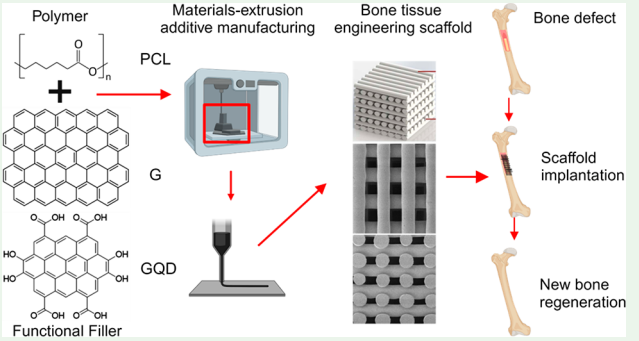

KEYWORDS: *additive manufacturing, bone tissue engineering, graphene, graphene quantum dot, polycaprolactone, scaffold*

1. INTRODUCTION

Large-scale bone loss raised by accidents, trauma, diseases, or tumor resection is a major clinical issue; thus, the treatment and consequent bone regeneration are critical, in which osteogenesis, osteoinduction, osteoconduction, and angiogenesis are the fundamental elements for successful bone reconstruction.[1] Current clinical therapeutic interventions for large-scale bone defects mainly focus on the application of metal implants or biological grafts including autografts, allografts, and xenografts. These methods present several limitations such as limited availability, rejection after implantation, affection on immunogenicity, and the transmission of diseases from donors to recipients.[2] These major problems usually lead to poor clinical outcomes.[3] 3D-printed synthetic material scaffolds present high reproducibility, interconnectivity, cytocompatibility, bioactivity, and anti-inflammation properties.[4,5] However, challenges such as optimal material selection allowing the optimal regeneration effect and cost control based on different methods still exist. Additionally, in-depth mechanism studies on how the material regulates genes and growth factors, as well as the safety of clinical applications, still require further investigation.[6] Nevertheless, they showed great potential to replace the current clinically utilized natural bone grafts and further enhance bone regeneration efficiency.[4,5,7] To realize the expected outcome, the scaffolds must meet different requirements, including adequate mechanical support close to the native bone

Received: November 1, 2023
Revised: December 8, 2023
Accepted: December 11, 2023
Published: January 3, 2024

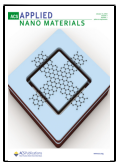

Scheme 1. Schematic Illustration of the Preparation Process of G, GQD, and Composite

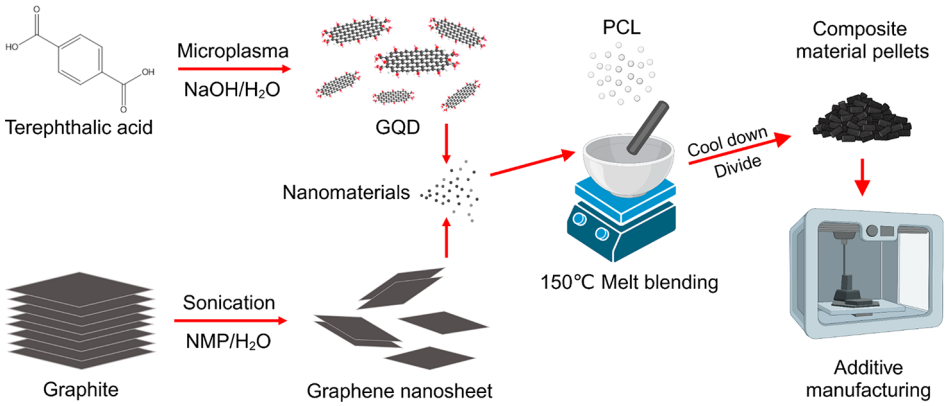

environment, biodegradability that matches the new bone regeneration rate, and the capability to stimulate vascularization, osteogenesis, and osteointegration, ultimately leading to rapid healing of bone tissue.[8,9]

Polycaprolactone (PCL), a synthetic polymeric material, has been widely used for scaffold fabrication due to its exceptional biocompatibility and biodegradability.[10−12] However, inadequate mechanical properties and bioactivity limit its application on its own in bone tissue engineering.[9,13−15] To address these limitations, many functional fillers have been considered, including graphene (G) and its derivatives such as reduced graphene oxide, graphene oxide, graphene quantum dots (GQD), and small hydrocarbon molecules.[16,17] With their excellent mechanical, chemical, and biological properties, these promising and desirable functional fillers present the ability to modulate and enhance the performance of polymeric scaffolds for bone tissue engineering.[16,17]

G is consisted of a two-dimensional structure of sp^2-hybridized carbon atoms arranged in a hexagonal shape.[18] Due to the high rigidity and electrical conductivity, the mechanical properties of the scaffolds can be significantly improved by adding a small amount of G.[18] The positive impact on cell−cell signaling also leads to the improvement of cell attachment, proliferation, and osteogenic differentiation.[9,19,20] The incorporation of G can also induce moderate levels of reactive oxygen species (ROS), essential for normal cellular functioning, but detrimental if produced in excess (the amount is cell-type specific).[9,21−24]

GQD, a nanomaterial derived from G with less than 100 nm in size, is regarded as the next-generation biomaterial.[25−27] Its special properties such as biocompatibility, chemical inertness, effective renal clearance, antioxidant, antimicrobial, and enticing photoluminescence (PL) properties offer vast possibilities in tissue engineering applications.[25−28] Incorporating GQD into the polymeric matrix can potentially enhance the mechanical properties of the resulting composites and provide responsive stimuli for sensing applications.[28,29] Applying GQD to hydrogels was also reported to promote *in vivo* bone tissue regeneration due to their capability to enhance stem cell differentiation.[30] More importantly, the smaller size of GQD relative to G makes it easier to be metabolized and excreted out of the body after entering *in vivo*, without affecting the host's cells.[31,32] This property offers a high possibility of integrating GQD with polymeric material for biodegradable scaffold fabrication.[31,32]

Multiple research has been conducted on G or other G-based materials reinforced scaffolds, while current investigation on GQD is limited to films and membranes (which cannot emulate complex *in vitro* and *in vivo* environments) rather than 3D structures or bone tissue engineering applications.[33−35] The information on comparing G and GQD under the same loading concentration to bone tissue engineering scaffolds is also extremely limited. This paper, for the first time, investigates and compares different loading levels of G and GQD for bone tissue engineering applications, particularly the engineering of 3D PCL bone tissue engineering scaffolds with a controlled architecture through additive manufacturing. Comprehensive studies were conducted to evaluate the morphological, chemical, surface, mechanical, and *in vitro* biological properties. Results fill a research gap by revealing the potential and feasibility of applying GQD to additively manufactured scaffolds for bone tissue engineering applications and ultimately facilitating the optimal design of future bone tissue engineering scaffolds.

2. MATERIALS AND METHODS

2.1. Material Preparation. PCL (Capa 6500, ≈50 kDa) was purchased in the form of 3 mm pellets from Ingevity (Warrington, UK). It presents the density of 1.1 g/cm^3, melting point between 58−60 °C, and glass transition temperature of around −60 °C under the standard conditions.

G nanosheets (3−4 layers, surface diameter of around 500 nm) were prepared through water-assisted liquid phase exfoliation of graphite as shown in Scheme 1. Briefly, a mixture of *N*-methyl-2-pyrotanone (NMP, 99% extra pure, Acros Organics, USA) containing 0.2 mass fractions of water was used to impregnate 50 mg of microcrystalline graphite powder (325 mesh, 99.995% pure, Alfa Aesar, UK). For exfoliation, the starting graphite concentration was set at 5 mg mL^{-1}.

The GQDs were synthesized from terephthalic acid (TPA, Sigma-Aldrich, UK), considering a home-built direct current Ar microplasma electrochemical reactor under ambient conditions, as previously reported[36,37] (Scheme 1). 0.1 M of TPA precursor solution was prepared by dissolving TPA in 0.3 M of NaOH. The obtained solution was then microplasma treated at 10 mA fixed discharge current for 30 min to synthesize the colloidal GQDs. After the reaction, the plasma-treated solution was subsequently neutralized with 1 M of hydrochloric acid and dialyzed (500−1000 D, Biotech CE Tubing, Spectrum Laboratories, Inc., USA) against deionized (DI) water for 1 day. DI water was replaced every 6 h. Afterward, the obtained solution was evaporated using a rotary evaporator (Eyela, Japan) operated at low pressure (<10 hPa) and low temperature (−10 °C). Approximately 50% of the sample vial was submerged in a water bath at 30 °C during this procedure. Once all the solution had been

https://doi.org/10.1021/acsanm.3c05225
ACS Appl. Nano Mater. 2024, 7, 1245−1256

evaporated, fine GQD powder was collected through a drying chamber overnight.

A physical melt blending method was used to prepare PCL/G and PCL/GQD composite material pellets at three different concentrations (1, 3, and 5 wt %) as shown in Scheme 1. Briefly, PCL pellets were heated to 150 °C, and then carbon nanomaterials were added at desired concentrations and mixed for 60 min to ensure an even dispersion. After 2 h of cooling, the mixed material was divided into small pellets ready for 3D printing.

2.2. Nanomaterial Characterization. The absorbance and PL measurements were conducted under ambient temperature, using a JASCO V676 absorbance spectrophotometer (JASCO, Japan) and a Nanolog-3 PL spectrofluorometer (HORIBA Scientific, Japan) equipped with a PMT detector (HORIBA Scientific, Japan), respectively. Both the GQD and G powders were dispersed in DI water with a concentration of 1 mg/mL followed by ultrasonication for 20 min. Afterward, 3 mL of sample suspensions were put in a quartz cuvette for PL measurements. A matching pair of quartz cuvettes with a 1 cm path length was used for the absorbance measurement. DI water was used to correct the baseline before every measurement. Raman measurements were conducted by using a JASCO 5100 spectrometer (JASCO, Japan) under green laser excitation (λ = 532 nm). Around 10 mg of GQD and G powders were first cast on two different glass slides. Then, each glass slide containing the Raman specimen was compressed with another clean glass slide to flatten the surface. The Raman shifts were calibrated to the Raman shifts of the Si wafer (520 cm^{-1}) prior to sample measurements. Transmission electron microscopy (TEM) measurements were conducted with a field emission gun TEM (JEOL JEM-2100F, Japan) considering a 200 kV accelerating voltage. The colloidal GQDs were drop-cast on a pure carbon copper grid (400 mesh, Ted Pella Inc., USA), while the G was drop-cast on a lacey copper grid (Ted Pella Inc., USA). X-ray diffraction (XRD) measurements were performed using a Bruker D8 DISCOVER SSS Multi-Function High Power XRD instrument (Bruker, USA). 10 mg of GQD and G powders were mounted on a glass flat sample plate for the XRD measurements.

2.3. Scaffold Design and Fabrication. A screw-assisted material-extrusion additive manufacturing system (3D Discovery, RegenHU, Switzerland) was used for scaffold fabrication. A 0°/90° fiber laying pattern was considered in order to achieve interconnected pores with regular square geometry. The considered processing parameters were a melting temperature of 90 °C, deposition velocity of 12 mm/s, screw rotation velocity of 8 rpm, and fiber diameter of 330 μm. All scaffolds were printed as 32.0 × 32.0 × 3.1 mm^3.

2.4. Thermogravimetric analysis (TGA). TGA was conducted with a Q500 thermogravimetric analyzer (TA Instruments, USA) considering samples of 6 ± 1 mg for each test. The experiment was carried out in the nitrogen atmosphere (gas flow of 90 mL/min) with temperatures ranging from 30 to 560 °C (temperature ramp of 10 °C/min). The final carbon material contents were determined by tracking the weight losses during the test.

2.5. Differential Scanning Calorimetry (DSC). The composite material crystallinity after scaffold fabrication was investigated via a Q100 Differential Scanning Calorimeter (TA Instrument, USA). All experiments were carried out in a nitrogen atmosphere considering a flow rate of 50 mL/min. Samples were first heated from −90 to 100 °C at a rate of 10 °C/min, rapidly cooled from 100 to −90 °C at 20 °C/min, and held at −90 °C for 2 min. Afterward, the second cycle was from −90 to 100 °C at 10 °C/min. The first heating process displays the thermal history following the printing process, which can be regarded as the thermal characteristics of the printed scaffolds, while the second heating process displays the thermal characteristics of the composite materials that are inherent to themselves after the removal of previous thermal history.[9] The crystallinity (%) was calculated as

$$\chi_C(\text{crystallinity}) = \frac{\Delta H_m}{\Delta H_m^0} \times \frac{100}{W} \quad (1)$$

where the melting enthalpy measured experimentally is ΔH_m, and ΔH_m^0 = 139.5 J/g is the enthalpy of melting 100% crystalline PCL.[12] The weight fraction of PCL in the composite material is expressed as W.

2.6. Morphological Characterization. The morphological analysis was conducted through scanning electron microscopy (SEM) using a TESCAN MIRA3 system (TESCAN, Czech). All scaffold samples were cut into 4.0 × 4.0 × 3.1 mm^3 and coated with gold−palladium (80:20) for 6 nm using a Q150T ES sputter coater (Quorum Technologies, UK) prior to imaging. The top surface and cross-section of each scaffold were imaged at an accelerating voltage of 2 kV accelerating voltage. ImageJ (NIH, USA) was used to process the collected pictures and calculate the scaffold fiber diameter, pore size, and porosity.

2.7. Nanoindentation Analysis. The surface hardness and reduced modulus of all scaffold samples were assessed through nanoindentation. HYSITRON TI 950 TriboIndentor (Bruker, USA) equipped with a typical three-sided pyramidal (Berkovich) probe was considered. A 5 mN load was used for the nanoindentation, resulting in a depth of around 2 μm. Twenty indents were conducted for each sample with a 50 μm gap between each other. The used profile was loading at 0.8 μN/s for 5 s, holding at the peak load (P_{max}) for 2s, and unloading at 0.8 μN/s for 5 s. Corresponding forces and displacements were recorded throughout the test. P_{max} and the contact area (A_c) were used to determine the hardness (H) through analysis software as follows:

$$H = \frac{P_{max}}{A_c} \quad (2)$$

Applying the Oliver−Pharr model and taking into account the contact stiffness (S) and A_c, the reduced modulus (E_r) was computed as follows:

$$E_r = \frac{S \times \sqrt{\pi}}{2 \times \sqrt{A_c}} \quad (3)$$

2.8. Apparent Water-in-Air Contact Angle (WCA) Measurement. The surface hydrophilicity of the scaffolds was evaluated by using the KRÜSS DSA 100 system (KRÜSS Instruments, Germany). A micrometric liquid dispenser (Hamilton, USA) was used to drop 1.7 μL of DI water onto the surface of the scaffold. Drop Shape Analysis (KRÜSS Instruments, Germany) software automatically records the image and determines the WCA using the sessile drop approach.

2.9. Mechanical Characterization. Uniaxial mechanical compression tests were carried out in order to evaluate the compressive modulus and strength of all fabricated scaffolds. Scaffold samples were cut into blocks of 3.0 × 3.0 × 3.1 mm^3 (h_0). The INSTRON 3344 testing system (Norwood, USA) fitted with a 100 N load cell was used for the test. The experiment was conducted in dry conditions. The rate of 0.5 mm/min and a strain limit of 0.2 mm/mm (20%) were considered. Force F and accompanying displacement values during the uniaxial compression were recorded, which were then transformed into engineering stress σ and strain ε as follows:

$$\sigma = \frac{F}{A} \quad (4)$$

$$\varepsilon = \frac{\Delta h}{h_0} \quad (5)$$

where Δh is the scaffold height change and A is the initial sample cross-section area. According to the technique described by Fiedler et al.,[38] the obtained stress−strain data were subsequently analyzed to determine the compressive modulus and compressive strength.

2.10. *In Vitro* Biological Characterization. Human adipose-derived stem cells (hADSCs, STEMPRO, Invitrogen, USA) of passages 3−5 were considered for *in vitro* biological characterization. MesenPRO RSTM Basal Medium (Invitrogen, USA) was used to culture cells in T75 flasks (Sigma-Aldrich, UK) until 80% confluence. At each time point, cells were harvested with 0.05% trypsin solution

https://doi.org/10.1021/acsanm.3c05225
ACS Appl. Nano Mater. 2024, 7, 1245−1256

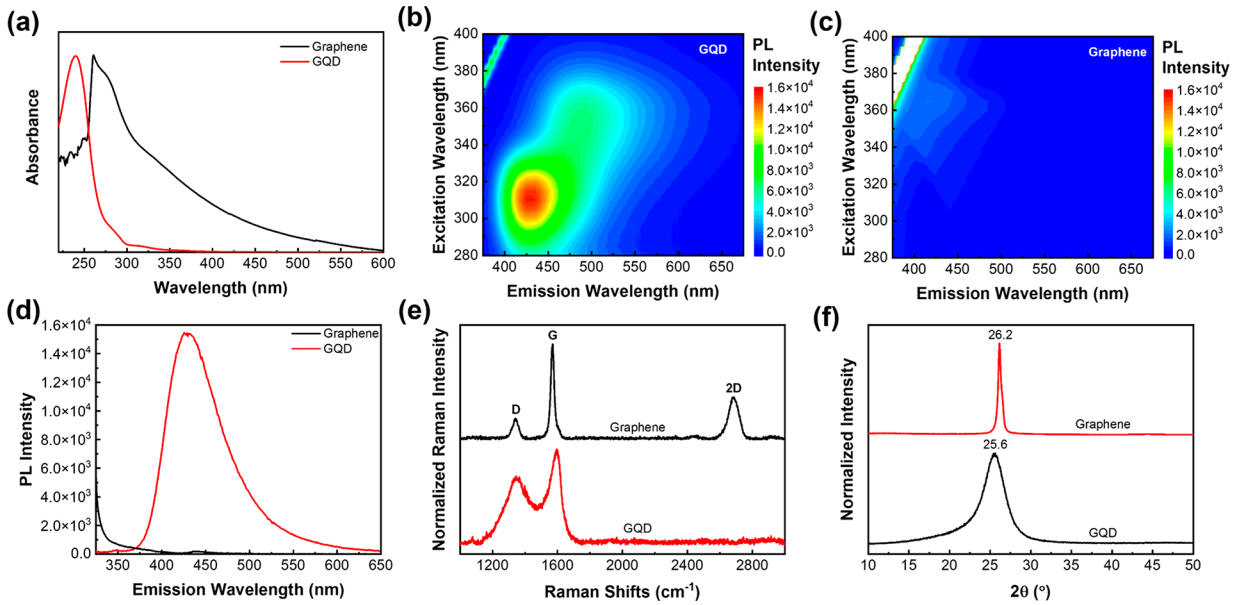

Figure 1. Characterization of GQD and G: (a) absorption spectra of both materials; PL maps of (b) GQD and (c) G; (d) PL spectra of both materials under 310 nm excitation wavelength (used to generate the strongest PL emission intensity of GQD); (e) Raman and (f) XRD spectra of GQD and G.

(Invitrogen, USA). Scaffold samples were cut to suit 48-well plates (Corning, USA), sterilized with 70% ethanol, washed with phosphate buffered saline (PBS) (Sigma-Aldrich, UK), and air-dried before cell seeding. Approximate 2.5 × 10^4 hADSCs were seeded on each scaffold sample. Standard conditions (37 °C, 5% CO_2, and 95% humidity) were applied for the incubation, and the culture medium was changed every 2 days throughout the biological assessment.

2.10.1. Cell Viability/Proliferation. The Alamar Blue test, also known as the Resazurin assay, was employed for assessing the cell viability/cytotoxicity and proliferation on all of the fabricated scaffold samples. Assessments were performed 1, 7, 14, and 21 days after cell seeding. During each assessment, the cell-seeded scaffolds were first transferred to a new 48-well plate, followed by the addition of 400 μL of culture medium containing 0.001% of the Alamar Blue solution (Invitrogen, USA) to each well. Afterward, samples were incubated for 4 h under standard conditions, with 150 μL of medium transferred to a 96-well plate (Corning, USA) at the end. The fluorescence intensity was measured at a 540 nm excitation wavelength and a 590 nm emission wavelength using a TECAN Infinite 200 (Tecan Group Ltd., Switzerland) plate reader.

2.10.2. Bioimaging. Cell spreading and qualitative adhesion statuses were further assessed through confocal microscopy imaging. On day 7 and 21, cell-seeded samples were rinsed twice with PBS, fixed with 10% paraformaldehyde (Sigma-Aldrich, UK) for 40 min, and then immersed in PBS containing 0.1% Triton X-100 (Sigma-Aldrich, UK) for 7 min. Subsequently, PBS containing 7% fetal bovine serum (FBS, Sigma-Aldrich, UK) was added for 30 min after rinsing twice in PBS. Afterward, cellular actin was stained using Alexa Fluor 594 Phalloidin (Invitrogen, USA) diluted to the manufacturer's recommended concentration (1:400) for 45 min in the dark. After rinsing twice in PBS, 4′,6-Diamidino-2-phenylindole dihydrochloride (DAPI) (Invitrogen, USA) was added to stained cell nuclei at the manufacturer's recommended concentration. Confocal images were obtained on a Leica SP8 LIGHTNING confocal microscope (Leica, Germany).

SEM imaging was also considered to evaluate cell attachment and proliferation on days 7 and 21. Before imaging, all cell-seeded scaffold samples were treated with 10% glutaraldehyde solution (Sigma-Aldrich, UK) for 45 min at room temperature, rinsed twice with PBS, dehydrated with graded ethanol series (50%, 70%, 80%, 90%, and 100% (twice)) with 10 min exposure at each step, followed by 50:50 ethanol/hexamethyldisilazane (HMDS, Sigma-Aldrich, UK), and last in 100% HMDS, and air-dried for HMDS removal. Prior to imaging, all samples were coated with 6 nm Gold−Palladium (80:20).

2.11. Data Analysis. In this research, all experiments were conducted with a minimum of three scientific repeats, and all experimental data were presented in the form of mean ± standard deviations. OriginLab (OriginLab Corporation, USA) was used for the data analysis considering one-way analysis of variance (one-way ANOVA) with *post hoc* Tukey's test. Significance levels were set at * $p < 0.05$, ** $p < 0.01$, and *** $p < 0.001$.

3. RESULTS AND DISCUSSION

3.1. Carbon Nanomaterial Characterization. The absorption spectra of both GQD and G are presented in Figure 1a. Different from G which exhibited an absorption shoulder around 277 nm, GQD exhibited a pronounced absorption peak at 240 nm, which can be ascribed to the $\pi-\pi^*$ transition of the C═C bond. The absorption tail from 270−400 nm, on the other hand, can be assigned to the n-π^* transition of oxygen containing functional groups. The PL phenomenon arising from the size quantization in GQD is distinctly proved by the PL measurements in Figure 1b and 1c. GQD demonstrated a wide range of PL emissions starting from 400−600 nm, with the strongest PL intensity located at 429 and 310 nm of emission and excitation wavelengths, respectively (Figure 1b). Contrarily, since G is a 2D carbon nanomaterial with zero band gap, it failed to show any PL emission (Figure 1c). Figure 1d presents the PL spectrum of GQD with the strongest intensity, and the result was compared with G. In addition, both GQD and G were subjected to microRaman measurements in order to investigate their vibrational structures. GQD possesses a more pronounced and broader D-band at 1346 cm^{-1} and a red-shifted G-band of about 25 cm^{-1} compared with that of G (Figure 1e). Note that the G-band represents the nonelastic vibration of sp^2 carbon, while the D-band is associated with the disorders in the form of vacancies, surface functional groups, and edge effects. The absence of 2D-band in the GQD can be attributed to its small particle size, rich functional groups, and possibly multilayered structure. To assess the crystallinity structure, XRD spectros-

https://doi.org/10.1021/acsanm.3c05225
ACS Appl. Nano Mater. 2024, 7, 1245−1256

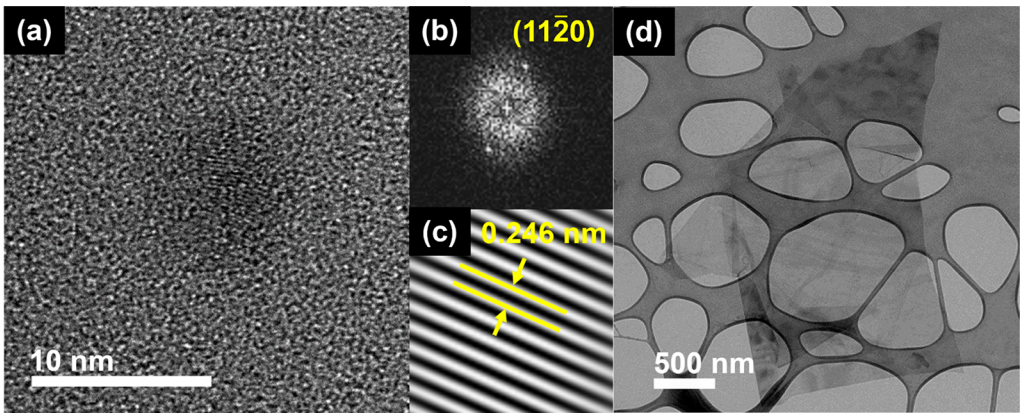

Figure 2. Morphological characterization of GQD and G: (a) HR-TEM; (b) FFT and (c) inverse FFT images of a single GQD particle; (d) TEM image of G.

copy measurements were performed on both GQD and G, and the results were compared. As shown in Figure 1f, a strong peak was observed at 26.2° for G which may be caused by the (002) diffraction pattern of C═C in the basal plane. However, it is apparent that the GQD shows a lower diffraction angle and broader peak at 25.6°, which may be contributed by the existence of vacancies and extensive surface functional groups.[39] This result is in accordance with the high D-band in the Raman spectrum of GQD.

TEM measurements were performed on both GQD and G in order to investigate their morphological structures. Figure 2a shows the high-resolution TEM image of a single GQD particle with its corresponding fast Fourier transform (FFT) image, presented in Figure 2b. The filtered inverse FFT image (Figure 2c) further revealed a lattice spacing of 0.246 nm corresponding to the diffraction pattern of G (11$\bar{2}$0, Figure 2b). Contrary to this, the TEM image of G presented in Figure 2d showed a sheet-like structure with a large surface area (>500 nm). These TEM results are consistent with the PL, Raman, and XRD results.

3.2. Thermal Analysis. *3.2.1. TGA.* The scaffold thermal decomposition temperature and carbon nanomaterial (G and GQD) content were evaluated using TGA. As shown in Table 1, both functional fillers were successfully integrated into the polymer matrix without considerable decomposition or weight loss during the material preparation and scaffold production processes, indicating that the considered temperatures of material preparation (150 °C) and printing (90 °C) are appropriate for scaffold fabrication.

Table 1. G and GQD Material Loading Verification, Assessed by TGA

Target carbon nanomaterial loading (wt %)	Determined carbon nanomaterial concentration (wt %)
0 (PCL)	–
1 (G)	1.06 ± 0.29
1 (GQD)	0.95 ± 0.21
3 (G)	2.93 ± 0.28
3 (GQD)	3.02 ± 0.67
5 (G)	4.84 ± 0.28
5 (GQD)	4.55 ± 0.56

3.2.2. DSC. DSC results (Table 2) suggested that adding both G and GQD to PCL slightly increased overall crystallinity after the scaffold fabrication, apart from the highest 5 wt % concentration (without statically difference). Polymer crystallization is a process of orderly accumulation of molecular chains.[40] High concentrations of carbon nanomaterials aggregate in the polymer matrix, hindering the movement of molecular chains and affecting the crystallization process.[40,41] Similar results were also reported by other researchers on polylactic acid (PLLA)/carbon nanotube scaffolds.[41] In addition, the reinforcement material in the polymer also serves as the nucleation site of the crystallization.[42,43] The number of nucleation sites typically dictates the morphology of the emerging microcrystals. An excessive amount of nucleation centers results in a significant number of small microcrystals, which may also lead to a lower crystallinity.[42,43] Notably, under the same concentration, G presented a slightly higher increasing impact than GQD. This may be attributed to the fact that G can provide more evident nucleation sites due to the larger particle size compared with GQD.[43] As researched, for semicrystalline polymeric materials, crystallinity affects the mechanical properties at both material microstructure and scaffold macrostructure levels; thus, the addition of these functional fillers presented a certain positive impact on the scaffold mechanical property.[44]

It was also observed that the glass transition temperature (T_g) from the first heating process were higher than those from the second heating process, showing that the printing process caused a delay in the polymer chain relaxation.[11] This could be attributed to the rotational effect of the screw-assisted printing system, which helps to form higher-order crystalline structures.[33] In the second heating process, the inclusion of G and GQD results in a minor increase in the T_g. The T_g of polymeric materials depends on multiple factors including crystallinity, molecular weight, density, and synthesis methods.[45] Physical properties of polymers, including viscosity, heat capacity, elastic modulus, Young's modulus, and coefficient of thermal expansion, also vary with T_g.[45,46]

3.3. Morphological Characterization. SEM images (both the top surface and cross-section) of all fabricated scaffolds are presented in Figure 3, and corresponding measurements are presented in Table 3. As illustrated, the printed scaffolds had regular square pores with an average pore size of 342.38 ± 28.19 μm vertically (top surface, designed value of 350 μm) and 178.69 ± 21.13 μm horizontally (cross-section, designed value of 210 μm), average fiber diameter of 342.22 ± 5.39 μm (designed value of 330 μm), and average porosity of 46.78 ± 0.83% (designed value of 46%), close to

https://doi.org/10.1021/acsanm.3c05225
ACS Appl. Nano Mater. 2024, 7, 1245−1256

Table 2. Thermal Characteristics of All Scaffold Materials[a]

Samples	T_g (°C)	T_m (°C)	ΔH_m (J/g)	χ_c (%)
		First Heating Process		
PCL	−66.49 ± 0.60	52.26 ± 0.66	105.17 ± 0.86	75.39 ± 0.62
PCL/G 1 wt %	−66.20 ± 0.52	53.05 ± 0.51	106.17 ± 4.33	76.87 ± 3.13
PCL/G 3 wt %	−65.80 ± 0.77	52.47 ± 0.55	107.87 ± 2.20	79.72 ± 1.62
PCL/G 5 wt %	−66.06 ± 0.44	52.29 ± 0.97	101.59 ± 2.18	76.66 ± 1.64
PCL/GQD 1 wt %	−66.01 ± 0.93	51.71 ± 0.60	105.83 ± 0.97	76.63 ± 0.70
PCL/GQD 3 wt %	−65.62 ± 0.28	51.56 ± 1.5	102.27 ± 1.39	75.58 ± 1.02
PCL/GQD 5 wt %	−64.66 ± 1.15	50.95 ± 0.31	94.63 ± 4.00	71.41 ± 3.02
		Second Heating Process		
PCL	−65.96 ± 0.96	49.94 ± 0.17	81.69 ± 0.65	58.56 ± 0.47
PCL/G 1 wt %	−66.36 ± 0.59	50.03 ± 0.14	83.09 ± 5.73	60.16 ± 4.15
PCL/G 3 wt %	−65.19 ± 0.41	49.47 ± 0.29	86.20 ± 1.48	63.70 ± 1.09
PCL/G 5 wt %	−66.70 ± 0.39	49.46 ± 0.23	81.11 ± 1.36	61.21 ± 1.03
PCL/GQD 1 wt %	−66.45 ± 0.24	50.36 ± 0.26	82.24 ± 4.00	59.55 ± 2.90
PCL/GQD 3 wt %	−66.01 ± 1.36	50.40 ± 0.24	83.39 ± 1.77	61.49 ± 1.31
PCL/GQD 5 wt %	−66.86 ± 0.55	50.42 ± 0.40	75.23 ± 2.46	56.77 ± 1.86

[a] T_m: melting temperature. ΔH_m: melt enthalpy. χ_c: crystallinity.

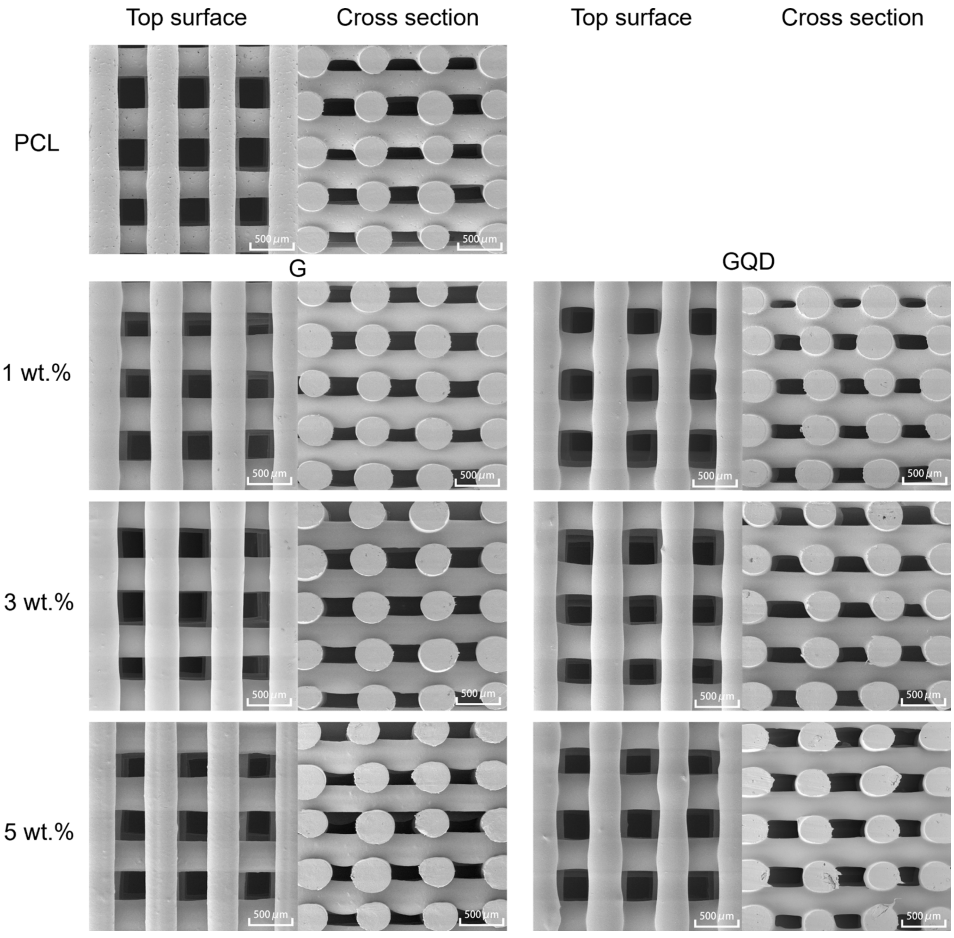

Figure 3. SEM images of the top surfaces and cross sections of all printed scaffolds.

the original design. Results confirmed that additive manufacturing presented excellent fabrication repeatability and strong control over the scaffold topology, which are essential factors for constructing three-dimensionally linked porous scaffolds (including pore size, shape, and pore distribution). Under the premise of ensuring mechanical properties matching human bone, the high porosity scaffold is important as it can better transport nutrients and oxygen, and promote cell attachment, proliferation, migration, and differentiation.[47] The general geometry structures and internal morphological structures were also proven to be similar among different material compositions, which was fundamental for all other mechanical and biological characterizations. The minor discrepancies between the measurement and design values could be attributed to the rheological effects (viscosity, shear

https://doi.org/10.1021/acsanm.3c05225
ACS Appl. Nano Mater. 2024, 7, 1245−1256

Table 3. Fiber Diameter, Pore Size, and Porosity Measurement Results of All Fabricated Scaffold

Scaffolds	Fiber diameter (μm)	Pore size (top surface) (μm)	Pore size (cross section) (μm)	Porosity (%)
Designed	330	350	210	46
PCL	336.06 ± 5.13	344.59 ± 6.85	156.20 ± 2.58	45.5 ± 0.15
1 wt % G	337.11 ± 0.03	332.22 ± 1.96	183.59 ± 3.90	46.9 ± 0.10
3 wt % G	347.24 ± 0.03	296.26 ± 1.87	207.22 ± 3.91	47.1 ± 0.05
5 wt % G	342.73 ± 1.92	327.71 ± 0.01	159.91 ± 1.95	47.4 ± 0.23
1 wt % GQD	340.58 ± 0.12	355.96 ± 17.07	164.43 ± 1.93	47.9 ± 0.04
3 wt % GQD	340.68 ± 0.21	387.43 ± 10.35	173.42 ± 1.95	45.9 ± 0.01
5 wt % GQD	351.14 ± 0.37	352.49 ± 5.16	206.08 ± 0.11	46.8 ± 0.13
Average	342.22 ± 5.39	342.38 ± 28.19	178.69 ± 21.13	46.78 ± 0.83%

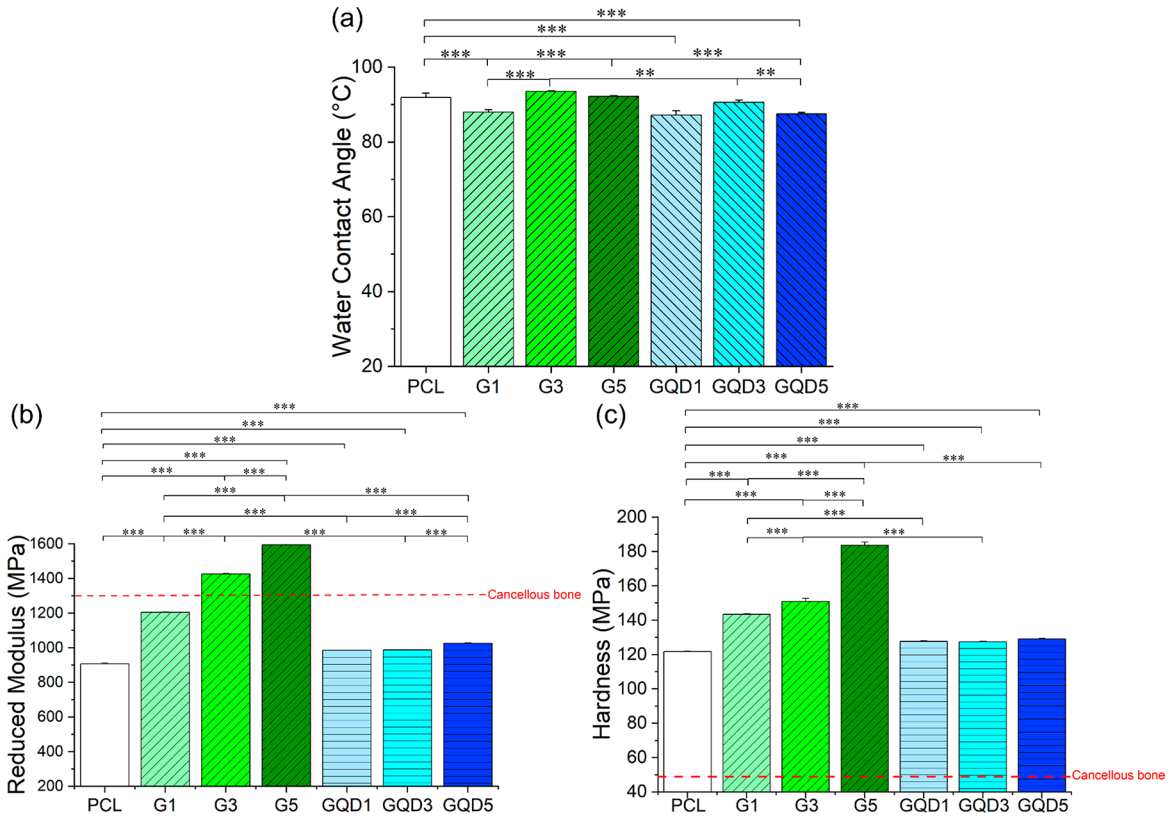

Figure 4. Surface characteristics include (a) WCA measurement results (time captured at 0 s), (b) reduced modulus, and (c) surface hardness of PCL, PCL/G, and PCL/GQD scaffolds.

deformation, and viscoelastic characteristics) associated with the various material compositions.

3.4. Surface Analysis. *3.4.1. Surface Hardness and Reduced Modulus.* As shown in Figure 4b and c, results suggested that, with the addition of G and GQD, both surface hardness and reduced modulus were greatly improved compared with those of PCL scaffolds. For the reduced modulus, statistical differences can be observed among PCL, PCL/G, and PCL/GQD groups at all material concentrations. Both PCL/G and PCL/GQD scaffolds showed an increasing trend proportional to G and GQD concentrations. Under the same concentration, PCL/G presented higher values compared with PCL/GQD. The reduced modulus of 3 wt % and 5 wt % G scaffolds matched the human cancellous bone (1.3−14.8 GPa).[48] In terms of the surface hardness, a similar trend was observed. Both PCL/G and PCL/GQD scaffolds presented significantly higher values than PCL scaffolds, and the increase was also proportional to the material concentration. The hardness of all scaffolds also matched the human cancellous bone (49−579 MPa).[49] Comparing G and GQD under the same concentration, PCL/G scaffolds showed higher values than PCL/GQD scaffolds in both surface hardness and reduced modulus. Differences in particle size at an order of magnitude level could be a main determinant.[43] Besides, the material crystallinity could be another reason. The capacity to support loads under high crystallinity is improved by the production of more and larger crystals.[44] Nanomechanical stimuli such as surface hardness and stiffness present a direct influence on the cell response. They first recognize sticky proteins on the substrate via transmembrane integrin receptors, receiving mechanical signals. The polymerization of actin fiber then activates and promotes focal adhesion, ultimately affecting cell proliferation and differentiation. Thus, higher surface hardness positively influences cell proliferation and differentiation.[50,51]

3.4.2. WCA. Figure 4a shows the WCA measurement results, indicating the surface wettability (values below 90° denote hydrophilicity, whereas values above 90° represent hydro-

https://doi.org/10.1021/acsanm.3c05225
ACS Appl. Nano Mater. 2024, 7, 1245−1256

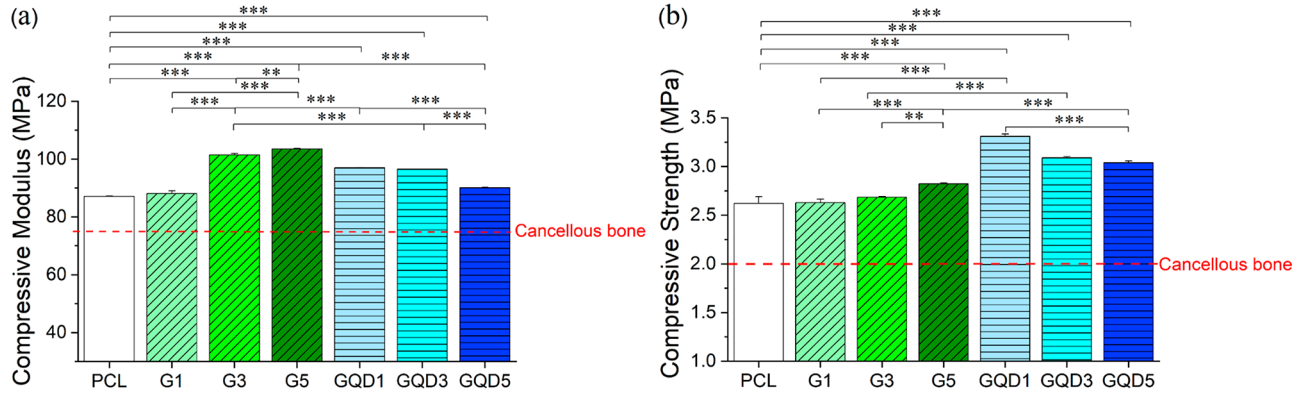

Figure 5. Mechanical characterization results including (a) the compressive modulus and (b) the compressive strength of all scaffold samples.

phobicity). Results suggested that PCL scaffolds presented a hydrophobic nature, reflected in the highest WCA value of 91.9° ± 1.18. The WCA values decreased with the addition of both G and GQD, where PCL/GQD scaffolds varied between 87.17° ± 1.19 (1 wt % GQD) and 90.63° ± 0.55 (3 wt % GQD), and PCL/G scaffolds varied between 87.96° ± 0.64 (1 wt % G) and 93.53° ± 0.12 (3 wt % G). The decrease may be due to the surface pattern raised by carbon nanomaterials that existed on the fiber surface. Besides, the agglomeration of carbon nanomaterials makes these surface patterns appear as three-dimensional blocks rather than two-dimensional nanosheets. Under the same concentration, the WCA value of PCL/GQD was lower than that of PCL/G. Changes in wettability, particularly in the case of GQD, could also be attributed to the presence of oxygenated functionalities on GQD nanosheets.[52] Similar results on G were also reported by Zhang et al.[53] They confirmed the hydrophilicity of ultraclean G membranes by measuring WCA using environmental SEM, and observed that the hydrophilicity arises from charge transfer between G and water molecules.[53] Generally, hydrophilic surfaces lead to increased protein adsorption, which plays an important role in cell attachment, proliferation, migration, osteoblastic differentiation, and osteoblast maturation.[17,54] However, surfaces that are superhydrophilic (0°) or superhydrophobic (above 150°) can lead to a sharp decline in cell adhesion.[55,56]

3.5. Mechanical Characterization. The mechanical property of PCL scaffolds was greatly improved with the addition of both G and GQD as shown in Figure 5. For the compressive modulus, PCL/G scaffolds presented a significantly increasing trend with the increase of G concentration. Conversely, as the GQD concentration increased, the PCL/GQD scaffold showed a decreasing trend in the compressive modulus. Similar results were also observed by other researchers upon incorporation of GQD into polymeric materials. The agglomeration of GQD at higher concentrations resulted in a decrease in the compressive modulus of the PCL/GQD scaffold.[35,57] Nevertheless, the compressive modulus of the 3 and 5 wt % PCL/G scaffolds (101.44 ± 0.45 and 103.54 ± 0.18 MPa respectively) and all PCL/GQD scaffolds (97.01 ± 0.05 to 90.15 ± 0.04 MPa) were still higher than that of the PCL scaffolds (87.08 ± 0.147 MPa).

Similarly, in terms of compressive strength, the PCL/G scaffold increased with G concentration (2.63 ± 0.04 to 2.82 ± 0.01 MPa), while the PCL/GQD scaffold decreased by increasing the GQD concentration (3.31 ± 0.02 MPa to 3.04 ± 0.02 MPa). The presence of well-dispersed rigid fillers restricts planar motion and elongation, which may lead to lower compressive modulus and compressive strength at the highest GQD concentration.[57] Nonetheless, the compressive strength of all PCL/GQD scaffolds remained significantly higher than those of PCL/G scaffolds and PCL scaffolds. Under the same concentration, PCL/GQD scaffolds presented higher compressive strength than PCL/G scaffolds, which could be attributed to GQD having a much larger edge area compared with G. Therefore, more covalent bonds could exist between carbon nanomaterial and the substrate (carbonyl, hydroxyl, and carboxyl) within the polymer matrix, which can transfer loads better.[57−59] Lastly, the obtained results also indicated that the produced scaffolds could provide adequate compressive strength and compressive modulus similar to human cancellous bone (compressive modulus of 75−435 MPa and compressive strength of 2−12 MPa).[60,61] Sufficient mechanical properties matching host bones are fundamental elements for a bone tissue engineering scaffold, in order to withstand hydrostatic and pulse pressures typical in the physiological environment, and maintain the space or pores required for cell attachment, proliferation, and differentiation.[51,62]

3.6. Biological Characterization. Figure 6 shows the cell viability/proliferation results. As observed, the fluorescence

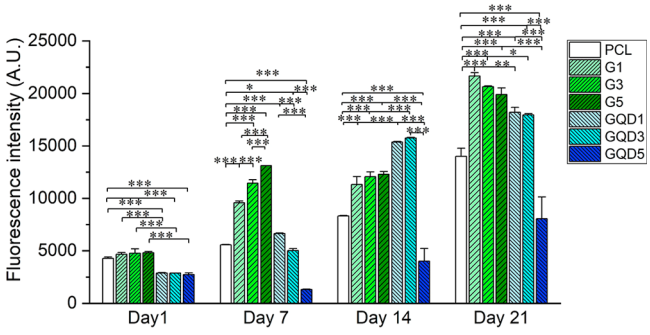

Figure 6. Cell viability/proliferation results (fluorescence intensity) of all fabricated scaffolds at days 1, 7, 14, and 21 of cell culture.

intensity (proportional to the amount of metabolically active cells, indicating the cell proliferation status) of all the cell-seeded scaffolds increased from the cell seeding to day 21, demonstrating the scaffolds' capability to create a suitable environment for cell proliferation without significant cytotoxicity, except for 5 wt % GQD scaffolds. 5 wt % GQD scaffolds showed a lower value compared with PCL scaffolds, indicating potential cytotoxicity due to the high functional filler addition.

https://doi.org/10.1021/acsanm.3c05225
ACS Appl. Nano Mater. 2024, 7, 1245−1256

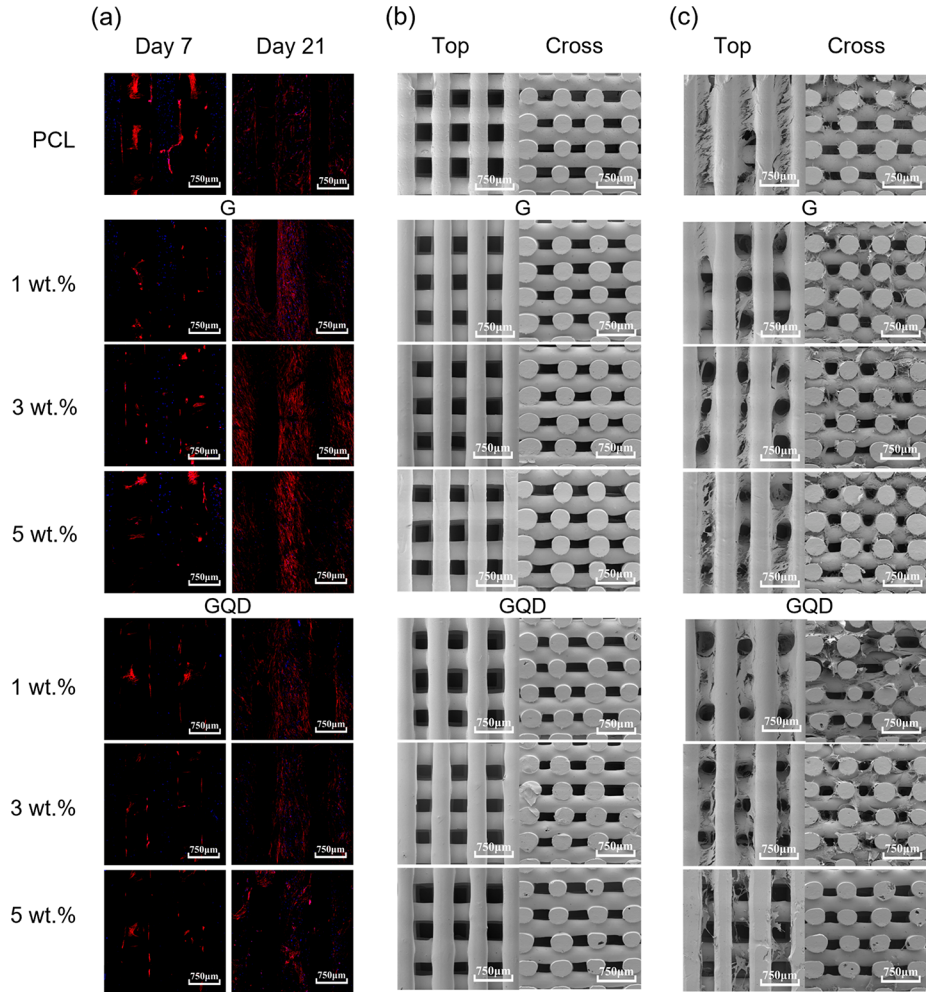

Figure 7. (a) Confocal microscopy images of all cell-seeded scaffolds (top surface, nuclei stained blue, and cell actin stained red) at day 7 and 21 of proliferation; (b–c) SEM images of all cell-seeded scaffolds (top surface and cross section) at day 7 and 21 of proliferation.

On day 1, no significant difference was observed between PCL and PCL/G scaffolds, while PCL/GQD scaffolds presented lower values than both groups. This may be attributed to the lower cell attachment rate resulting from the lower WCA values and less significant surface patterning effect compared with PCL/G scaffolds due to the smaller particle size.

Starting from day 7, the positive impact of the functional material addition became dominant. All PCL/G scaffolds showed statistically higher fluorescence intensities than PCL scaffolds, 1 wt % PCL/GQD scaffolds as well. This positive impact could be attributed to carbon nanomaterials enhancing cell–cell signaling and releasing moderate levels of ROS which influenced the cellular functioning on the scaffold, promoting cell proliferation.[9,21,63] The negative effect on cell proliferation from the highest GQD concentration (5 wt %) may be attributed to the rapid dispersion effect due to the smaller particle size, rapidly entering the cell membrane to decompose, affecting intercellular signaling. Such impact was also reported by Liang et al. using molecular dynamics simulation.[64]

From day 14 and onward, all PCL/G and PCL/GQD scaffolds (except 5 wt % GQD) exhibited significantly higher fluorescence intensities than PCL scaffolds, and all scaffolds almost achieved full confluency on day 21. For all PCL/G scaffolds and 1 and 3 wt % PCL/GQD scaffolds, the fluorescence intensity increased with G or GQD concentrations, continuously higher than the PCL group. Notably, it was observed that on day 14 the fluorescence intensity of the 1 and 3 wt % PCL/GQD scaffolds were significantly higher than that of the PCL/G scaffolds at the same concentration, but PCL/G scaffolds presented higher cell proliferation results on day 21. This may be because PCL/GQD groups achieved confluency earlier. All of the above-mentioned results suggested that the addition of both carbon nanomaterials promoted the proliferation of hADSCs, but different threshold values were identified between the maximum positive effect and triggering cytotoxicity. Under the same concentration of carbon nanomaterial addition, the PCL/GQD scaffold showed slightly higher proliferation results at the early stage, while the PCL/G scaffold performed better in the longer term (21 days). At lower concentrations, GQD presented advantages in terms of faster endocytosis and metabolization effect to G, improved cell–cell signaling, and introduced moderate levels of ROS, facilitating faster proliferation. While at higher concentrations, the negative effect of smaller GQD overcame the positive impact, more likely to pierce the cell membrane thus causing cell necrosis.[21] Considering the enhancement effect, GQD showed a stronger and faster effect at lower concentrations.

Both confocal microscopy and SEM images (Figure 7) were considered to evaluate the cell attachment and proliferation

https://doi.org/10.1021/acsanm.3c05225
ACS Appl. Nano Mater. 2024, 7, 1245–1256

statuses after 7 and 21 days. Imaging results demonstrated that the scaffolds sustained cell growth along the orientation of the fibers. As observed, from day 7 to day 21, confluent cells widely adhered and spread on the scaffolds, bridging between the fibers. Images further demonstrated that PCL/G and PCL/GQD scaffolds showed superior confluency as well as cell distribution in comparison to PCL scaffolds.

4. CONCLUSIONS

This research investigated the use of additive manufacturing for the fabrication of PCL/G (GQD) 3D bone tissue engineering scaffolds and evaluated the effect of adding G and GQD as functional fillers on their morphological, mechanical, chemical, surface, and *in vitro* biological properties. PCL/G and PCL/GQD materials were efficiently mixed by a physical melt blending process, and a screw-assisted additive manufacturing system successfully fabricated the scaffolds with precise control of the morphological structure and without a significant loss of carbon nanomaterial. The evaluation showed that the addition of G and GQD improved surface wettability, mechanical properties, and *in vitro* biological performance of the scaffolds. In terms of mechanical property, PCL/G scaffolds showed higher compressive modulus, reduced modulus, and surface hardness, while the PCL/GQD scaffold showed a higher compressive strength. Significant improvement in the scaffold biological performance was observed in terms of supporting hADSC proliferation (cellular metabolic activity). A potential cytotoxic effect from 5 wt % GQD addition was also observed. These results (abiotic and biotic properties) contribute to the optimization of future bone tissue engineering scaffold design. Future research will focus on long-term *in vitro* cell differentiation assays considering bone regeneration related protein expression, alkaline phosphate, and alizarin red S staining, using human bone marrow mesenchymal stem cells. Additionally, *in vivo* studies on animal models, including whole-body bioluminescent imaging, hematoxylin-eosin staining, and Masson staining, will be conducted. In addition, *in vitro* degradation experiments of the scaffolds will be performed to observe the changes in mechanical and surface properties, as well as functional filler release.

AUTHOR INFORMATION

Corresponding Author

Weiguang Wang − *School of Engineering, Faculty of Science and Engineering, The University of Manchester, Manchester, U.K. M13 9PL;* orcid.org/0000-0002-8959-329X; Email: weiguang.wang@manchester.ac.uk

Authors

Duo Meng − *School of Engineering, Faculty of Science and Engineering, The University of Manchester, Manchester, U.K. M13 9PL*

Yanhao Hou − *School of Engineering, Faculty of Science and Engineering, The University of Manchester, Manchester, U.K. M13 9PL;* orcid.org/0000-0001-9229-0356

Darwin Kurniawan − *Department of Chemical Engineering, National Taiwan University of Science and Technology, Taipei, Taiwan 10607;* orcid.org/0000-0003-4198-7641

Ren-Jie Weng − *Department of Chemical Engineering, National Taiwan University of Science and Technology, Taipei, Taiwan 10607*

Wei-Hung Chiang − *Department of Chemical Engineering, National Taiwan University of Science and Technology, Taipei, Taiwan 10607;* orcid.org/0000-0002-6350-6696

Complete contact information is available at: https://pubs.acs.org/10.1021/acsanm.3c05225

Author Contributions

Conceptualization, D.M., Y.H., W.W.; methodology, D.M., Y.H., W.W.; formal analysis, D.M., Y.H., W.W.; investigation, D.M., Y.H., R.J.W., W.W.; writing—original draft preparation, D.M., Y.H., D.K., W.W.; writing—review and editing, D.M., Y.H., W.H.C., W.W.; supervision, W.W. All authors have read and agreed to the published version of the manuscript.

Author Contributions

[§]D.M. and Y.H. contributed equally to this work.

Notes

The authors declare no competing financial interest.

ACKNOWLEDGMENTS

The authors wish to acknowledge Rosetrees Trust UK and Stoneygate Trust UK for the Enterprise Fellowships (ref: M874).

REFERENCES

(1) e Silva, E. P.; Huang, B.; Helaehil, J. V.; Nalesso, P. R. L.; Bagne, L.; de Oliveira, M. A.; Albiazetti, G. C. C.; Aldalbahi, A.; El-Newehy, M.; Santamaria-Jr, M.; Mendonça, F. A. S.; Bártolo, P.; Caetano, G. F. In vivo study of conductive 3D printed PCL/MWCNTs scaffolds with electrical stimulation for bone tissue engineering. *Bio-Design and Manufacturing* **2021**, *4* (2), 190−202.

(2) Vidal, L.; Kampleitner, C.; Brennan, M. Á.; Hoornaert, A.; Layrolle, P. Reconstruction of Large Skeletal Defects: Current Clinical Therapeutic Strategies and Future Directions Using 3D Printing. *Frontiers in Bioengineering and Biotechnology* **2020**, *8*, 61.

(3) Koh, A.; Kang, D.; Xue, Y.; Lee, S.; Pielak, R. M.; Kim, J.; Hwang, T.; Min, S.; Banks, A.; Bastien, P.; Manco, M. C.; Wang, L.; Ammann, K. R.; Jang, K.-I.; Won, P.; Han, S.; Ghaffari, R.; Paik, U.; Slepian, M. J.; Rogers, J. A. (**2016**) A soft, wearable microfluidic device for the capture, storage, and colorimetric sensing of sweat. *Science Translational Medicine*, *8* (366). DOI: 10.1126/scitranslmed.aaf2593.

(4) Hassan, M.; Khaleel, A.; Karam, S. M.; Al-Marzouqi, A. H.; Ur Rehman, I.; Mohsin, S. Bacterial Inhibition and Osteogenic Potentials of Sr/Zn Co-Doped Nano-Hydroxyapatite-PLGA Composite Scaffold for Bone Tissue Engineering Applications. *Polymers* **2023**, *15* (6), 1370.

(5) Sarkar, N.; Bose, S. Controlled release of soy isoflavones from multifunctional 3D printed bone tissue engineering scaffolds. *Acta Biomaterialia* **2020**, *114*, 407−420.

(6) Xue, N.; Ding, X.; Huang, R.; Jiang, R.; Huang, H.; Pan, X.; Min, W.; Chen, J.; Duan, J.-A.; Liu, P.; Wang, Y. Bone Tissue Engineering in the Treatment of Bone Defects. *Pharmaceuticals* **2022**, *15* (7), 879.

(7) Hou, Y.; Wang, W.; Bartolo, P. Application of additively manufactured 3D scaffolds for bone cancer treatment: A review. *Bio-Design and Manufacturing* **2022**, *5* (3), 556−579.

(8) Mohammadi Zerankeshi, M.; Bakhshi, R.; Alizadeh, R. Polymer/metal composite 3D porous bone tissue engineering scaffolds fabricated by additive manufacturing techniques: A review. *Bioprinting* **2022**, *25*, No. e00191.

(9) Wang, W.; Huang, B.; Byun, J. J.; Bártolo, P. Assessment of PCL/carbon material scaffolds for bone regeneration. *Journal of the Mechanical Behavior of Biomedical Materials* **2019**, *93*, 52−60.

(10) Meng, Z.; He, J.; Cai, Z.; Wang, F.; Zhang, J.; Wang, L.; Ling, R.; Li, D. Design and additive manufacturing of flexible polycaprolactone scaffolds with highly-tunable mechanical properties for soft tissue engineering. *Materials & Design* **2020**, *189*, 108508.

(11) Lopes Nalesso, P. R.; Wang, W.; Hou, Y.; Bagne, L.; Pereira, A. T.; Helaehil, J. V.; Moretti De Andrade, T. A.; Chiarotto, G. B.; Bártolo, P.; Caetano, G. F. In vivo investigation of 3D printed polycaprolactone/graphene electro-active bone scaffolds. *Bioprinting* **2021**, *24*, No. e00164.
(12) Hou, Y.; Wang, W.; Bartolo, P. Investigation of polycaprolactone for bone tissue engineering scaffolds: In vitro degradation and biological studies. *Materials & Design* **2022**, *216*, 110582.
(13) Zhang, K.; Fan, Y.; Dunne, N.; Li, X. Effect of microporosity on scaffolds for bone tissue engineering. *Regenerative Biomaterials* **2018**, *5* (2), 115−124.
(14) Budi, H. S.; Anitasari, S.; Shen, Y.-K.; Tangwattanachuleeporn, M.; Nuraini, P.; Setiabudi, N. A. Novel Application of 3D Scaffolds of Poly(E-Caprolactone)/Graphene as Osteoinductive Properties in Bone Defect. *European Journal of Dentistry* **2022**, s-0042−1755550.
(15) Hou, Y.; Wang, W., Bartolo, P. Investigating the Degradation Properties of Poly(ε-caprolactone) and Polyethylene Terephthalate Glycol as Biomaterials. In *Progress in Digital and Physical Manufacturing*; Correia Vasco, J. O., de Amorim Almeida, H., Gonçalves Rodrigues Marto, A., Bento Capela, C. A., da Silva Craveiro, F. G., Coelho da Rocha Terreiro Galha Bártolo, H. M., de Jesus Coelho, L. M., Simões Correia, M. A., Nogueira Vieira, M. M., Barreiros Ruben, R. M., Eds.; Springer International Publishing: 2023; pp 379−387.
(16) Cheng, J.; Liu, J.; Wu, B.; Liu, Z.; Li, M.; Wang, X.; Tang, P.; Wang, Z. Graphene and its Derivatives for Bone Tissue Engineering: In Vitro and In Vivo Evaluation of Graphene-Based Scaffolds, Membranes and Coatings. *Frontiers in Bioengineering and Biotechnology* **2021**, *9*, 734688.
(17) Anitasari, S.; Wu, C.-Z.; Shen, Y.-K. PCL/Graphene Scaffolds for the Osteogenesis Process. *Bioengineering* **2023**, *10* (3), 305.
(18) Seabra, A. B.; Paula, A. J.; De Lima, R.; Alves, O. L.; Durán, N. Nanotoxicity of Graphene and Graphene Oxide. *Chem. Res. Toxicol.* **2014**, *27* (2), 159−168.
(19) Hou, Y.; Wang, W.; Bartolo, P. J. D. S. Investigating the Effect of Carbon Nanomaterials Reinforcing Poly(E-Caprolactone) Scaffolds for Bone Repair Applications. *International Journal of Bioprinting* **2020**, *6* (2), 266.
(20) Hou, Y.; Wang, W.; Bártolo, P. Novel Poly(ε -caprolactone)/Graphene Scaffolds for Bone Cancer Treatment and Bone Regeneration. *3D Printing and Additive Manufacturing* **2020**, *7* (5), 222.
(21) Yuan, X.; Zhang, X.; Sun, L.; Wei, Y.; Wei, X. Cellular Toxicity and Immunological Effects of Carbon-based Nanomaterials. *Particle and Fibre Toxicology* **2019**, *16* (1), 18.
(22) Milkovic, L.; Cipak Gasparovic, A.; Cindric, M.; Mouthuy, P.-A.; Zarkovic, N. Short Overview of ROS as Cell Function Regulators and Their Implications in Therapy Concepts. *Cells* **2019**, *8* (8), 793.
(23) Abdal Dayem, A.; Hossain, M.; Lee, S.; Kim, K.; Saha, S.; Yang, G.-M.; Choi, H.; Cho, S.-G. The Role of Reactive Oxygen Species (ROS) in the Biological Activities of Metallic Nanoparticles. *International Journal of Molecular Sciences* **2017**, *18* (1), 120.
(24) Hou, Y.; Wang, W.; Bartolo, P. The effect of graphene and graphene oxide induced reactive oxygen species on polycaprolactone scaffolds for bone cancer applications. *Materials Today Bio* **2024**, *24*, 100886.
(25) Haque, E.; Kim, J.; Malgras, V.; Reddy, K. R.; Ward, A. C.; You, J.; Bando, Y.; Hossain, Md. S. A.; Yamauchi, Y. Recent Advances in Graphene Quantum Dots: Synthesis, Properties, and Applications. *Small Methods* **2018**, *2* (10), 1800050.
(26) Barati, F.; Avatefi, M.; Moghadam, N. B.; Asghari, S.; Ekrami, E.; Mahmoudifard, M. A review of graphene quantum dots and their potential biomedical applications. *Journal of Biomaterials Applications* **2023**, *37* (7), 1137−1158.
(27) Pan, D.; Zhang, J.; Li, Z.; Wu, M. Hydrothermal Route for Cutting Graphene Sheets into Blue-Luminescent Graphene Quantum Dots. *Adv. Mater.* **2010**, *22* (6), 734−738.
(28) Dutta, K.; Sarkar, K.; Karmakar, S.; Gangopadhyay, B.; Basu, A.; Bank, S.; De, S.; Das, B.; Das, M.; Chattopadhyay, D. Asymmetric fabrication and *in vivo* evaluation of the wound healing potency of electrospun biomimetic nanofibrous scaffolds based on collagen crosslinked modified-chitosan and graphene oxide quantum dot nanocomposites. *J. Mater. Chem. B* **2023**, *11* (39), 9478−9495.
(29) Laysandra, L.; Kurniawan, D.; Wang, C.-L.; Chiang, W.-H.; Chiu, Y.-C. Synergistic Effect in a Graphene Quantum Dot-Enabled Luminescent Skinlike Copolymer for Long-Term pH Detection. *ACS Appl. Mater. Interfaces* **2021**, *13* (50), 60413−60424.
(30) Geng, B.; Fang, F.; Li, P.; Xu, S.; Pan, D.; Zhang, Y.; Shen, L. Surface charge-dependent osteogenic behaviors of edge-functionalized graphene quantum dots. *Chemical Engineering Journal* **2021**, *417*, 128125.
(31) Henna, T. K.; Pramod, K. Graphene quantum dots redefine nanobiomedicine. *Materials Science and Engineering: C* **2020**, *110*, 110651.
(32) Campbell, E.; Hasan, Md. T.; Gonzalez Rodriguez, R.; Akkaraju, G. R.; Naumov, A. V. Doped Graphene Quantum Dots for Intracellular Multicolor Imaging and Cancer Detection. *ACS Biomaterials Science & Engineering* **2019**, *5* (9), 4671−4682.
(33) Qiu, J.; Li, D.; Mou, X.; Li, J.; Guo, W.; Wang, S.; Yu, X.; Ma, B.; Zhang, S.; Tang, W.; Sang, Y.; Gil, P. R.; Liu, H. Effects of Graphene Quantum Dots on the Self-Renewal and Differentiation of Mesenchymal Stem Cells. *Adv. Healthcare Mater.* **2016**, *5* (6), 702−710.
(34) Khabibullin, A.; Alizadehgiashi, M.; Khuu, N.; Prince, E.; Tebbe, M.; Kumacheva, E. Injectable Shear-Thinning Fluorescent Hydrogel Formed by Cellulose Nanocrystals and Graphene Quantum Dots. *Langmuir* **2017**, *33* (43), 12344−12350.
(35) Sarabiyan Nejad, S.; Razzaghi, D.; Rezaei, M.; Bagheri, M.; Babaie, A.; Abbasi, F. Preparation and characterization of electrospun shape memory polyurethane/graphene quantum dot nanocomposite scaffolds for tissue engineering. *International Journal of Polymeric Materials and Polymeric Biomaterials* **2022**, *71* (14), 1069−1077.
(36) Yang, J.-S.; Pai, D. Z.; Chiang, W.-H. Microplasma-enhanced synthesis of colloidal graphene quantum dots at ambient conditions. *Carbon* **2019**, *153*, 315−319.
(37) Chiang, W.-H.; Richmonds, C.; Sankaran, R. M. Continuous-flow, atmospheric-pressure microplasmas: A versatile source for metal nanoparticle synthesis in the gas or liquid phase. *Plasma Sources Science and Technology* **2010**, *19* (3), 034011.
(38) Fiedler, T.; Videira, A. C.; Bártolo, P.; Strauch, M.; Murch, G. E.; Ferreira, J. M. F. On the mechanical properties of PLC-bioactive glass scaffolds fabricated via BioExtrusion. *Materials Science and Engineering: C* **2015**, *57*, 288−293.
(39) Das, R.; Parveen, S.; Bora, A.; Giri, P. K. Origin of high photoluminescence yield and high SERS sensitivity of nitrogen-doped graphene quantum dots. *Carbon* **2020**, *160*, 273−286.
(40) Shuai, C.; Zan, J.; Qi, F.; Wang, G.; Liu, Z.; Yang, Y.; Peng, S. nMgO-incorporated PLLA bone scaffolds: Enhanced crystallinity and neutralized acidic products. *Materials & Design* **2019**, *174*, 107801.
(41) Wang, G.; Qi, F.; Yang, W.; Yang, Y.; He, C.; Peng, S.; Shuai, C. Crystallinity and Reinforcement in Poly-L-Lactic Acid Scaffold Induced by Carbon Nanotubes. *Advances in Polymer Technology* **2019**, *2019*, 1−10.
(42) Park, C.-S.; Lee, K.-J.; Kim, S. W.; Lee, Y. K.; Nam, J.-D. Crystallinity morphology and dynamic mechanical characteristics of PBT polymer and glass fiber-reinforced composites. *J. Appl. Polym. Sci.* **2002**, *86* (2), 478−488.
(43) Park, C.-S.; Lee, K.-J.; Nam, J.-D.; Kim, S.-W. Crystallization kinetics of glass fiber reinforced PBT composites. *J. Appl. Polym. Sci.* **2000**, *78* (3), 576−585.
(44) Song, F.; Wang, Q.; Wang, T. The effects of crystallinity on the mechanical properties and the limiting PV (pressure × velocity) value of PTFE. *Tribiol. Int.* **2016**, *93*, 1−10.
(45) Zhang, Y.; Xu, X. Machine learning glass transition temperature of polymers. *Heliyon* **2020**, *6* (10), No. e05055.
(46) Catalan, K. N.; Corrales, T. P.; Forero, J. C.; Romero, C. P.; Acevedo, C. A. Glass Transition in Crosslinked Nanocomposite

https://doi.org/10.1021/acsanm.3c05225
ACS Appl. Nano Mater. 2024, 7, 1245−1256

Scaffolds of Gelatin/Chitosan/Hydroxyapatite. *Polymers* **2019**, *11* (4), 642.
(47) Kanwar, S.; Vijayavenkataraman, S. Design of 3D printed scaffolds for bone tissue engineering: A review. *Bioprinting* **2021**, *24*, No. e00167.
(48) XE, G. Is trabecular bone tissue different from cortical bone tissue? *Forma* **1997**, *12*, 185−196.
(49) WEAVER, J. K. The microscopic hardness of bone. *JBJS* **1966**, *48* (2), 273−288.
(50) Huang, B.; Wang, Y.; Vyas, C.; Bartolo, P. Crystal Growth of 3D Poly(ε -caprolactone) Based Bone Scaffolds and Its Effects on the Physical Properties and Cellular Interactions. *Advanced Science* **2023**, *10* (1), 2203183.
(51) Chung, S.; King, M. W. Design concepts and strategies for tissue engineering scaffolds. *Biotechnology and Applied Biochemistry* **2011**, *58* (6), 423−438.
(52) Deka, M. J.; Dutta, A.; Chowdhury, D. Tuning the wettability and photoluminescence of graphene quantum dots *via* covalent modification. *New J. Chem.* **2018**, *42* (1), 355−362.
(53) Zhang, J.; Jia, K.; Huang, Y.; Liu, X.; Xu, Q.; Wang, W.; Zhang, R.; Liu, B.; Zheng, L.; Chen, H.; Gao, P.; Meng, S.; Lin, L.; Peng, H.; Liu, Z. Intrinsic Wettability in Pristine Graphene. *Adv. Mater.* **2022**, *34* (6), 2103620.
(54) Gittens, R. A.; Scheideler, L.; Rupp, F.; Hyzy, S. L.; Geis-Gerstorfer, J.; Schwartz, Z.; Boyan, B. D. A review on the wettability of dental implant surfaces II: Biological and clinical aspects. *Acta Biomaterialia* **2014**, *10* (7), 2907−2918.
(55) Dowling, D. P.; Miller, I. S.; Ardhaoui, M.; Gallagher, W. M. Effect of Surface Wettability and Topography on the Adhesion of Osteosarcoma Cells on Plasma-modified Polystyrene. *Journal of Biomaterials Applications* **2011**, *26* (3), 327−347.
(56) Arima, Y.; Iwata, H. Effect of wettability and surface functional groups on protein adsorption and cell adhesion using well-defined mixed self-assembled monolayers. *Biomaterials* **2007**, *28* (20), 3074−3082.
(57) Gobi, N.; Vijayakumar, D.; Keles, O.; Erogbogbo, F. Infusion of Graphene Quantum Dots to Create Stronger, Tougher, and Brighter Polymer Composites. *ACS Omega* **2017**, *2* (8), 4356−4362.
(58) Dreyer, D. R.; Park, S.; Bielawski, C. W.; Ruoff, R. S. The chemistry of graphene oxide. *Chem. Soc. Rev.* **2010**, *39* (1), 228−240.
(59) Stankovich, S.; Dikin, D. A.; Piner, R. D.; Kohlhaas, K. A.; Kleinhammes, A.; Jia, Y.; Wu, Y.; Nguyen, S. T.; Ruoff, R. S. Synthesis of graphene-based nanosheets via chemical reduction of exfoliated graphite oxide. *Carbon* **2007**, *45* (7), 1558−1565.
(60) Morgan, E. F.; Unnikrisnan, G. U.; Hussein, A. I. Bone Mechanical Properties in Healthy and Diseased States. *Annu. Rev. Biomed. Eng.* **2018**, *20* (1), 119−143.
(61) Öhman-Mägi, C.; Holub, O.; Wu, D.; Hall, R. M.; Persson, C. Density and mechanical properties of vertebral trabecular bone—A review. *JOR SPINE* **2021**, *4* (4), No. e1176.
(62) Mohammadi Zerankeshi, M.; Bakhshi, R.; Alizadeh, R. Polymer/metal composite 3D porous bone tissue engineering scaffolds fabricated by additive manufacturing techniques: A review. *Bioprinting* **2022**, *25*, No. e00191.
(63) Wang, W.; Chen, J.-X.; Hou, Y.; Bartolo, P.; Chiang, W.-H. Investigations of Graphene and Nitrogen-Doped Graphene Enhanced Polycaprolactone 3D Scaffolds for Bone Tissue Engineering. *Nanomaterials* **2021**, *11* (4), 929.
(64) Liang, L.; Kong, Z.; Kang, Z.; Wang, H.; Zhang, L.; Shen, J.-W. Theoretical Evaluation on Potential Cytotoxicity of Graphene Quantum Dots. *ACS Biomaterials Science & Engineering* **2016**, *2* (11), 1983−1991.

https://doi.org/10.1021/acsanm.3c05225
ACS Appl. Nano Mater. 2024, 7, 1245−1256